







Article

Corrosion Behavior and Mechanical Properties of Zn–Ti Alloys as Biodegradable Materials

Alexandra-Tamara Şutic ¹, Romeu Chelariu ^{1,*}, Ramona Cimpoesu ¹, Ana-Maria Roman ¹, Bogdan Istrate ², Viorel Goanță ², Marcelin Benchea ², Mihaela Moscu ^{3,*}, Adrian Alexandru ¹, Nicanor Cimpoesu ¹ and Georgeta Zegan ⁴

¹ Department of Materials Science, Faculty of Materials Science and Engineering, “Gheorghe Asachi” Technical University of Iasi, 41 Dimitrie Mangeron Blvd., 700050 Iasi, Romania;

alexandra-tamara.sutic@student.tuiasi.ro (A.-T.Ş.); ramona.cimpoesu@academic.tuiasi.ro (R.C.);

ana-maria.roman@academic.tuiasi.ro (A.-M.R.); adrian.alexandru@academic.tuiasi.ro (A.A.);

nicanor.cimpoesu@academic.tuiasi.ro (N.C.)

² Faculty of Mechanical Engineering, “Gheorghe Asachi” Technical University of Iasi, 43 Dimitrie Mangeron Blvd., 700050 Iasi, Romania; bogdan.istrate@academic.tuiasi.ro (B.I.); viorel.goanta@academic.tuiasi.ro (V.G.); marcelin.benchea@academic.tuiasi.ro (M.B.)

³ Department of Morpho-Functional Sciences I, Faculty of Medicine, “Grigore T. Popa” University of Medicine and Pharmacy, 16 University Street, 700115 Iasi, Romania

⁴ Department of Surgical, Faculty of Dental Medicine, “Grigore T. Popa” University of Medicine and Pharmacy, 16 University Street, 700115 Iasi, Romania; georgeta.zegan@umfiasi.ro

* Correspondence: romeu.chelariu@academic.tuiasi.ro (R.C.); mihaela.moscu@umfiasi.ro (M.M.)

Abstract: The influence of the chemical composition and structural state of Zn–Ti alloys on corrosion behaviour and mechanical properties was studied. Zn-based alloys were investigated, more precisely, pure technical Zn and Zn with 0.10, 0.25 and 1.00 wt.% Ti. The microstructure and chemical composition of these materials were analysed using light optical microscopy (LOM), scanning electron microscopy (SEM), energy dispersive X-ray spectroscopy (EDS) and X-ray diffraction (XRD). The chemical composition of the alloys and the surface after immersion were analysed using an EDS detector from Bruker. The alloys’ electro-chemical corrosion resistance was further investigated through linear (LP) and cyclic (CP) potentiometry and open-circuit potential (OCP) analysis. A tensile/compression equipment (Instron 34SC-5) was used to determine the compression behaviour. UMT testing equipment was used to determine microhardness (by Rockwell indentation) and COF vs. length. For percentages higher than 0.25 wt.% Ti, the formation of a primary TiZn₁₆ intermetallic compound in the (α -Zn + TiZn₁₆) eutectic matrix was observed, a slight influence of TiZn₁₆ on the Zn corrosion resistance results, and a greater influence on the mechanical properties was confirmed.

Keywords: Zn–Ti biodegradable alloy; corrosion resistance; degradation rate



Citation: Şutic, A.-T.; Chelariu, R.; Cimpoesu, R.; Roman, A.-M.; Istrate, B.; Goanță, V.; Benchea, M.; Moscu, M.; Alexandru, A.; Cimpoesu, N.; et al. Corrosion Behavior and Mechanical Properties of Zn–Ti Alloys as Biodegradable Materials. *Metals* **2024**, *14*, 764. <https://doi.org/10.3390/met14070764>

Academic Editor: Mosab Kaseem

Received: 4 June 2024

Revised: 17 June 2024

Accepted: 21 June 2024

Published: 27 June 2024



Copyright: © 2024 by the authors. Licensee MDPI, Basel, Switzerland. This article is an open access article distributed under the terms and conditions of the Creative Commons Attribution (CC BY) license (<https://creativecommons.org/licenses/by/4.0/>).

1. Introduction

There are three main classes of biodegradable metals: Mg-, Fe- and Zn-based materials [1,2]. Although Mg-based materials have compatible mechanical properties with bone tissue and high osteopromotive and biocompatible behaviour during degradation, their biomedical applications are limited by their high degradation rate, which can cause both local gas accumulation and loss of mechanical integrity before the surrounding bone is fully healed [3]. Currently, Mg-based biodegradable materials are being used in the manufacture of commercial coronary stents and bone screws and pins [1,4,5]. For Fe-based materials, best machinability, excellent mechanical properties and cost-effectiveness are the main advantages as biodegradable materials; however, they have a slow degradation rate in the bone environment, and therefore, research has mainly focused on cardiovascular applications [1–4,6]. So far, there are no commercially available Fe-based materials on the global market, and their development is expected to require more time as their performance

depends on the complexity of their interactions with the physiological environment [6]. Investigations on Zn-based materials for biomedical applications have only recently emerged as a result of the favourable biodegradability characteristics in physiological environments, which are intermediate between those of Mg and Fe biodegradable metals [2,4]. Although the role of Zn in structural, catalytic and signalling processes is thoroughly proven and the human body has developed its own homeostatic capacity to maintain tight regulation of zinc levels in relation to its essentiality/toxicity duality [7,8], both deficiency and excess of Zn levels are associated with many disease conditions in the human body [9–11]. Despite its physiological relevance, Zn is not usually considered a first choice as a biodegradable medical material, corresponding to less than 100 publications in the last decade [3]. Even under these conditions, Zn-based materials have a great potential for clinical applications, such as biodegradable vascular scaffolds and bone implants, when considering their favourable association of mechanical properties, degradation behaviour and biocompatibility [4,12]. However, no clinical use of Zn-based orthopaedic devices has been reported [2].

Chen et al. [13] summarised both the issues and the perspectives of Zn-based materials for orthopaedic internal fixation implants. The study showed that biodegradable Zn-based materials have great potential for application as temporary implants for internal osteosynthesis due to their versatility, which can be modified and controlled by both chemical composition and processing, mechanical properties, degradation behaviour, biocompatibility and bacteriostatic activity. Furthermore, it has been shown that there are still important concerns, such as the correlation of the degradation rate with the tissue healing and the toxic dose of Zn^{2+} level, the stress corrosion and corrosion fatigue behaviour, the high longitudinal elastic modulus compared to the bone tissue and the creep effect at physiological human body temperature [7,13].

During the decades of Zn-based biodegradable material development, various strategies have been employed to improve their performance, but all have resulted in modifications of the microstructural features. Alloying has been widely used, namely for binary, tertiary, quaternary and quinary alloys, using different chemical elements [14–21]. By alloying and casting, the main microstructural features consist of a dendritic Zn-based solid solution as the primary phase (matrix) and secondary phases, often intermetallic compounds, formed by various reactions [22]. Thermomechanical processing can provide a further improvement in performance by altering the microstructural features (grain size, texture, phase volume fraction ratio, phase morphology, etc.), resulting in enhanced mechanical properties, degradation behaviour and biocompatibility [16–21].

As far as the binary Zn–Ti system has been studied, only a few studies have been conducted towards its use as a biodegradable material. In his master's thesis, Yin [23] extensively investigated some Zn–Ti alloys with Ti = 0.01, 0.1 and 0.03 wt.% as biodegradable materials for stents. The study showed the best combination of tensile properties for the hot-extruded Zn-0.1 wt.% Ti alloy without testing the corrosion and degradation behaviour, the friction and wear performance or the biocompatibility of these Zn–Ti alloys. Wang et al. [24] extended their investigations on some Zn–Ti alloys (Ti contents of 0.05, 0.1, 0.2 and 0.3 wt.%, cast + hot-rolled processing) by a comprehensive evaluation of their corrosion and degradation properties, friction and wear behaviour and in vitro cytotoxicity, motivated by the consideration that a high Ti ion concentration was toxic to osteoblast-like SaOS₂ cells, and the threshold of the Ti ion concentration was 15.5 µg/L. It was concluded that the microstructure was formed from an α -Zn matrix and a TiZn₁₆ intermetallic phase, with increased Ti content causing microstructural modifications and improved mechanical properties, higher corrosion current densities and higher corrosion rates, improved wear behaviour and no cytotoxicity to MG-63 cells for extracts with Ti ion concentrations \leq 25%.

In this work, some cast binary Zn–xTi alloys with specific contents of $x = 0.00, 0.10, 0.25$ and 1.00 wt.% have been studied regarding the relationship of their chemical composition and processing with their microstructural features and, hence, with their mechanical properties, degradation behaviour and frictional behaviour in order to determine their availability as biodegradable materials for temporary internal osteosynthesis implants.

Although various Zn alloy systems have been investigated, in the present study, the binary Zn–Ti alloy system was chosen in consideration of (i) the availability of the Zn–Ti phase diagram, (ii) the design of the cast Zn–Ti alloy and (iii) the potential of Ti as an alloying element to induce changes in microstructural features and, hence, significant changes in mechanical properties, degradation rate and biocompatibility.

2. Materials and Methods

2.1. Materials

A two-step laboratory-scale processing pathway was used: The first was the synthesis of a Zn-5 wt.% Ti master alloy (Zn-5Ti_{ma}) from ingots of commercially pure Zn (cp-Zn, 99.99 wt.%, each impurity < 0.005 wt.%) and Ti sponge (Tisp, 99.90 wt.%, each impurity < 0.02 wt.%), and the second was the synthesis of the targeted Zn-*x*Ti alloys, *x* = 0.00 wt.%, 0.10 wt.%, 0.25 wt.% and 1.00 wt.%, using cp-Zn and necessary quantities from Zn-5Ti_{ma}. To perform melting and alloying, both for the master alloy and targeted alloys, an induction furnace with an argon protective atmosphere and a silicon carbide crucible were used (medium frequency static generator, 20 kW/8 kHz/300 V, Electrotehnica SA Bucharest, București, Romania). The melted material (casting temperature approximately 600 °C) was poured into a metal mould preheated at 225 °C (cooling rate approximately 3–4 °C/s until the melt was completely solidified), then held in the mould for 10 min and finally extracted and air cooled. The primary ingots of the Zn-*x*Ti alloys had approximately 500 g and dimensions of 25 mm × 40 mm × 70 mm.

The primary ingots were subjected to mechanical and, where necessary, electroerosion processing to produce the final samples. After removing the upper part of the primary ingots, secondary ingots measuring 25 mm × 25 mm × 70 mm were processed and used to produce the four semi-finished samples (12 mm × 12 mm × 70 mm). The samples were used to characterise the microstructure, mechanical properties and the corrosion, wear and friction behaviour. Samples measuring 12 mm × 12 mm × 5 mm were prepared for microstructural characterisation. For the mechanical compression tests (10 mm × 12 mm) and for corrosion and degradation behaviour (10 mm × 5 mm), the samples were produced by electroerosion cutting and turning. A further set of specimens was prepared for micro-indentation testing to investigate the friction characteristics. To determine the chemical compositions of the investigated materials, the energy dispersive spectroscopy (EDS) method was used and performed on the grinded and polished samples (see Section 2.2) using an X-ray energy dispersive detector (energy dispersive spectroscopy (EDS), Bruker, X-Flash 6-10, Billerica, MA, USA, working mode in Esprit 2.2 for spectrum acquisition: automatic mode and Mapping).

2.2. Microstructure Analysis

To observe and analyse microstructure features, the samples were subjected to conventional preparation methods, mechanical grinding (SiC disks, P80-P2400 grit), mechanical polishing (alumina suspension, 1.00 μm, 0.30 μm, 0.04 μm) and an etchant containing 50 g CrO₃, 4 g Na₂SO₄ and 1000 mL H₂O, either alone or, where it was necessary, in combination with an etchant containing 5 g FeCl₃, 10 mL HCl and 240 mL alcohol.

Optical microscopy (OM) was performed using an ISM-M1000 Namicon (INSIZE, Suzhou, China) trinocular inverted mass metallographic microscope equipped with a MotiCam camera (10+, 10.0 MP) specialised in microscopic analysis and Motic Images Plus 3.0 (×86) software (version 3.0.12.41, Motic, China Group Co., Ltd. 2015, Hong Kong, China). For scanning electron microscopy (SEM), a VegaTescan LMH II (TESCAN, Brno-Kohoutovice, Czech Republic) microscope was used with a cathode supply voltage of 30 kV, secondary electron detector and working distance of 15.5 mm.

The X-ray diffraction analysis (XRD) was performed using an Xpert PRO MPD 3060 diffractometer from PANalytical (Almelo, The Netherlands) with a Cu X-ray tube ($K\alpha = 1.54051 \text{ \AA}$), $2\theta = 25^\circ\text{--}75^\circ$, step size = 0.13, time/step: 99.45 s and scan speed of $0.033667^\circ/\text{s}$ with a number of 3808 steps. The XRD patterns were analysed and phases

indexed using MATCH! Software version 3.16 Build 288 (Crystal Impact, Bonn, Germany). The samples for X-ray diffraction analysis (XRD) were not etched.

2.3. Mechanical Testing

Compressive testing was performed on an INSTRON 8801 testing machine (Norwood, MA, USA) (maximum load 100 kN). The compression samples were strained with a traverse speed (TS) = -0.68×10^{-3} mm/s up to a strain of 0.85. To evaluate the surface hardness, the microindentation tests on a CETR-UMT-2 tribometer were performed (Campbell, Camden, NJ, USA) using a Rockwell diamond tip (Milwaukee, WI, USA) (radius 200 μm and angle 120° , and a vertical load of 10 N). The results were interpreted using the Test Viewer software (version 2.16).

2.4. Corrosion and Degradation Behavior

2.4.1. Immersion Testing

The samples were immersed in a NaCl solution (9 mg/mL) in a thermostatically controlled enclosure at 37°C (20 mL/cm² ratio). For each immersion interval (3, 7 and 14 days), the degradation rate (DR) based on the mass loss was obtained for all Zn-xTi alloys. The samples were weighed using an AS220 Partner analytical balance (RADWAG Balances & Scales, Radom, Poland). The samples were subjected to ultrasonic cleaning in technical alcohol using an ultrasonic equipment (PRO 50 ASonic, Ultrasonic Cleaner, Beijing, China) for 60 min. The DRs [mm/y] were obtained according to ASTM G31-21 using the following equation [25], where W = mass loss [g]; A = sample area [cm²]; t = time [h] and ρ = density [g/cm³]:

$$\text{DR} = \frac{8.76 \times 10^4 \times W}{A \times t \times \rho} \quad (1)$$

In addition, the pH of the NaCl solution was registered for the first 72 h with a Hanna HI98191 (Darmstadt, Germany) pH meter equipped with a HI72911B titanium-bodied pH electrode and a temperature sensor that were inserted into the sample container during the experiment. The pH calibration was performed regularly at five points with pre-programmed standard buffer solutions with pH of 4.01; 6.86; 7.00; 9.18 and 10.01, achieving a pH accuracy of ± 0.002 to ± 0.001 . The data were acquired minute-by-minute using the Hanna HI-92000 software (version 5.0.38) with a USB connection.

2.4.2. Electrochemical Testing

A VoltaLab-21 potentiometer (Radiometer, Copenhagen, Denmark) was used to determine the corrosion resistance by analysing linear and cyclic potentiometry in NaCl as the electrolyte solution. The acquisition and processing of data were performed using the Volta Master 4 software (version 6.0.25130). A three-electrode cell was used to analyse the corrosion behaviour. A sample with an exposed surface of 0.63 cm² was used as the working electrode. A saturated calomel electrode (SCE) was used as a reference, and a platinum electrode was used as an auxiliary.

The solution was stirred with a magnetically driven, Teflon-coated stirring bar to remove hydrogen. Potentiodynamic polarisation curves were obtained at a scanning rate of 1 mV/s, and cyclic voltammetry curves were obtained at a scan rate of 10 mV/s. For linear potentiometry, scanning was performed in the range 500–1200 mV vs. FREE. The open circuit potential (OCP) was registered for 10 min before the electrochemical tests.

2.5. Friction Behavior Test

To evaluate friction behaviour, microscratch tests were performed using a CETR-UMT-2 tribometer (Campbell, Camden, NJ, USA). The tests involved a sharp stylus to produce a controlled and continuous microscratch mark on the material surface. Additionally, the AE signals provided information on the load-displacement characteristics during the microscratch test, helping to identify damage initiation and failure mechanisms. Two types

of microscratch tests were performed: one with a constant load and the other with a linearly increasing force. The tests were performed with vertical forces of 10 N and 19 N, moving the table 10 mm in 60 s at a rate of 0.167 mm/s. A widia cutting blade with a tip radius of 0.4 mm was used for the microscratch tests.

2.6. Statistical Analysis

For the mechanical, immersion corrosion and friction testing, the tests were replicated three times under the same testing conditions for all Zn–xTi alloys. To demonstrate the effect of the Ti content on the properties of the Zn–xTi alloys, the experimental data were statistically analysed using either one-way repeated measures ANOVA (OWR-ANOVA) or two-way repeated measures ANOVA (TWR-ANOVA), performed by Tukey’s test at a significance level of 0.05.

All experimental activities of this study have been conducted in accordance with the principles of occupational health and safety, the use of compliant instrumentation and machinery and proper personal protective equipment [26].

3. Results

3.1. Chemical Composition

The chemical compositions of the investigated Zn-based materials were determined using EDS and are shown in Table 1.

Table 1. Chemical compositions of the Zn–xTi biodegradable materials.

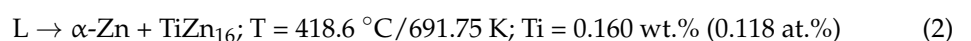
Element Average (St. Dev.) (wt.%)	Zn–xTi Alloys			
	Zn–0.00Ti	Zn–0.10Ti	Zn–0.25Ti	Zn–1.00Ti
Zn	99.99 (0.001)	99.814 (0.028)	99.663 (0.037)	99.007 (0.013)
Ti	-	0.113 (0.025)	0.259 (0.037)	0.910 (0.011)
Al	0.003 (0.002)	0.015 (0.002)	0.014 (0.004)	0.016 (0.002)
Ni	-	0.016 (0.002)	0.013 (0.001)	0.019 (0.003)
Si	-	0.013 (0.001)	0.019 (0.003)	0.013 (0.001)
Cu	0.002 (0.001)	0.015 (0.002)	0.015 (0.002)	0.014 (0.004)
Fe	0.004 (0.001)	0.014 (0.004)	0.016 (0.002)	0.019 (0.003)
Sn	0.002 (0.001)	-	-	-

3.2. Microstructure

3.2.1. Zn–Ti Phase Diagram and Alloy Design

It is well-known that, by adding small quantities of Ti into Zn-based alloys, a grain refinement effect and a change in the eutectic morphology are produced in correlation with the cooling rate of the melt [27–35]. In addition, the grain size can be controlled by the cooling rate of the melt, as Leone et al. [30] reported. For example, at 0.004–0.009 wt.% Ti for all cooling rates, a completely columnar microstructure was observed, but for 0.1 wt.% Ti and a 0.5 °C/s cooling rate, a small columnar microstructure was observed in contrast with a completely grain-refined microstructure observed at a cooling rate greater than 5 °C/s. To limit the grain-refinement effect determined by either the cooling rate or between the Ti wt.% content and the cooling rate, a 3–4 °C/s range value for the last was maintained for all Zn–xTi alloys. In contrast with other Zn–X phase diagrams, e.g., Zn–Al, the Zn–Ti phase diagram is still in dispute [35], especially the crystal structures of the low melting temperature compounds that are formed at the Zn-rich zone of the Zn–Ti phase diagram [25,36].

Ti has a very low solubility in Zn at room temperature, approximately 0.0004–0.0005 wt.% (0.00055–0.00068 at.%) Ti [31,37,38], and at 0.160 wt.% (0.118 at.%) Ti content, a eutectic reaction has been reported [24,27–36]:



The Ti content corresponding to the eutectic reaction is dependent on the cooling rate, with a 0.18 wt.% (0.25 at.%) value at a very low crystallisation rate [37]. Ti solubility in Zn depends on the temperature, thus at 300 °C, it varies in the 0.007–0.015 wt.% range (0.0095–0.0204 at.%), and at 400 °C, it is approximately 0.02 wt.% (0.027 at.%) [38].

The TiZn₁₆ intermetallic compound formed with an α -Zn eutectic, shown above, has an approximate 4.39 wt.% (5.90 at.%) Ti content [32,34]. According to the Ti–Zn phase diagram [28,31,34,39] and the chemical compositions of the Zn–xTi alloys (Figure 1), the main microstructural features for the four Zn–xTi alloys are as follows: (i) Zn–0.00Ti contains only α -Zn phase; (ii) Zn–0.10Ti, a hypoeutectic alloy, forms from α -Zn phase as a dendritic matrix and (α -Zn + TiZn₁₆) eutectic; (iii) Zn–0.25Ti, a hyper-eutectic alloy very close to the eutectic Ti content, contains an α -Zn + TiZn₁₆ eutectic and primary TiZn₁₆ (presumably with a low volume fraction); and (iv) Zn–1.00Ti, a hyper-eutectic alloy with a Ti content distant from the eutectic concentration, contains an α -Zn + TiZn₁₆ eutectic and primary TiZn₁₆ (presumably with a higher volume fraction and modified morphology).

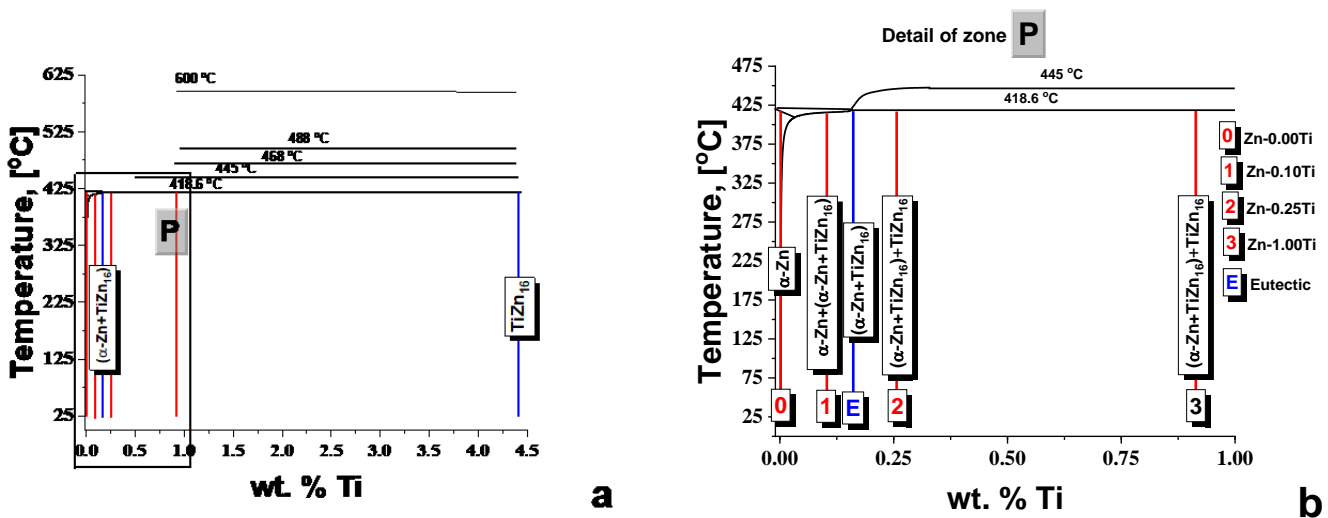


Figure 1. Details of the Zn–Ti phase diagram for wt.% Ti intervals of interest (adapted from Refs. [28,31,34,39]): (a) 0.00–4.5 wt.% Ti corresponding to TiZn₁₆ content area; (b) the wt.% Ti content for the Zn–xTi alloys.

3.2.2. XRD Analysis

The experimental XRD patterns are shown in Figure 2. According to the Zn–Ti phase diagram (Figure 1) [28,31,34,39], the phases formed are α -Zn (space group P6₃/mmc (194)) and TiZn₁₆ intermetallic compound (space group Cmc_m (63)) [34].

To index the diffractograms, the Match! software as well as the XRD standard patterns from the Crystallography Open Database (COD) and the literature data were used [31,36,40–42]. The lattice parameters for the two phases are as follows: (i) α -Zn, $a = 2.6648 \text{ \AA}$, $b = 4.4967 \text{ \AA}$ (COD Entry 96-900-8523); (ii) TiZn₁₆, $a = 7.7200 \text{ \AA}$, $b = 11.4490 \text{ \AA}$, $c = 11.7550 \text{ \AA}$ (COD Entry 96-210-6429). Match! software provides phase composition based on the experimental XRD pattern. Thus, the volume percentage of the TiZn₁₆ phase was (i) 2.7% for Zn–0.10Ti; (ii) 7.6% for Zn–0.25Ti and (iii) 20.3% for Zn–1.00Ti.

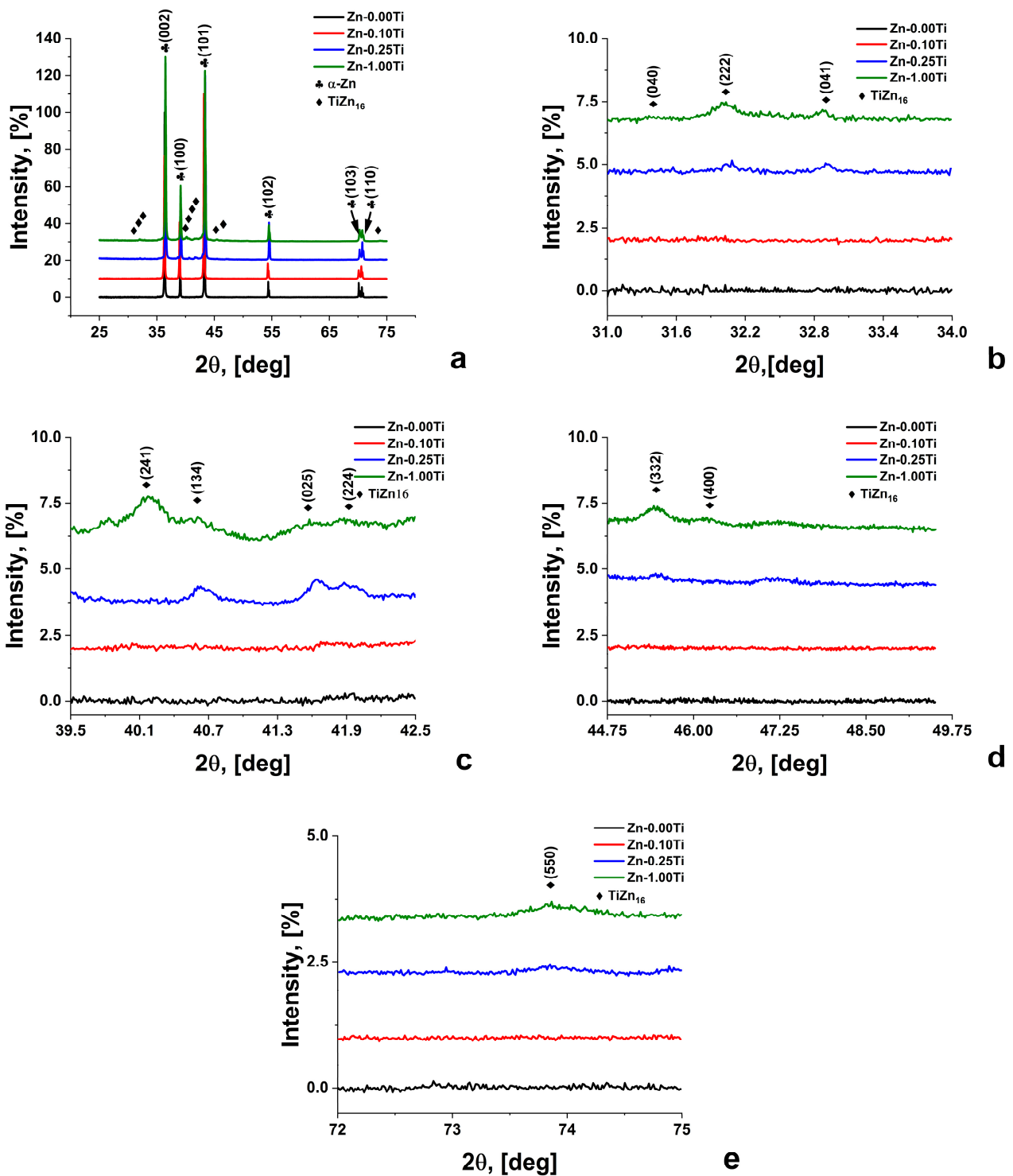


Figure 2. XRD patterns of Zn- x Ti alloys (2θ): (a) 25° – 75° for α -Zn; (b) 31° – 34° for TiZn_{16} ; (c) 39.5° – 42.5° for TiZn_{16} ; (d) 44.75° – 49.75° for TiZn_{16} ; (e) 72° – 75° for TiZn_{16} .

3.2.3. Optical Microscopy

Figure 3a–d show the optical microstructure (OM) of the Zn- x Ti alloys. The as-cast Zn-0.00Ti contains large grains (above $500\ \mu\text{m}$), as shown in Figure 3a.

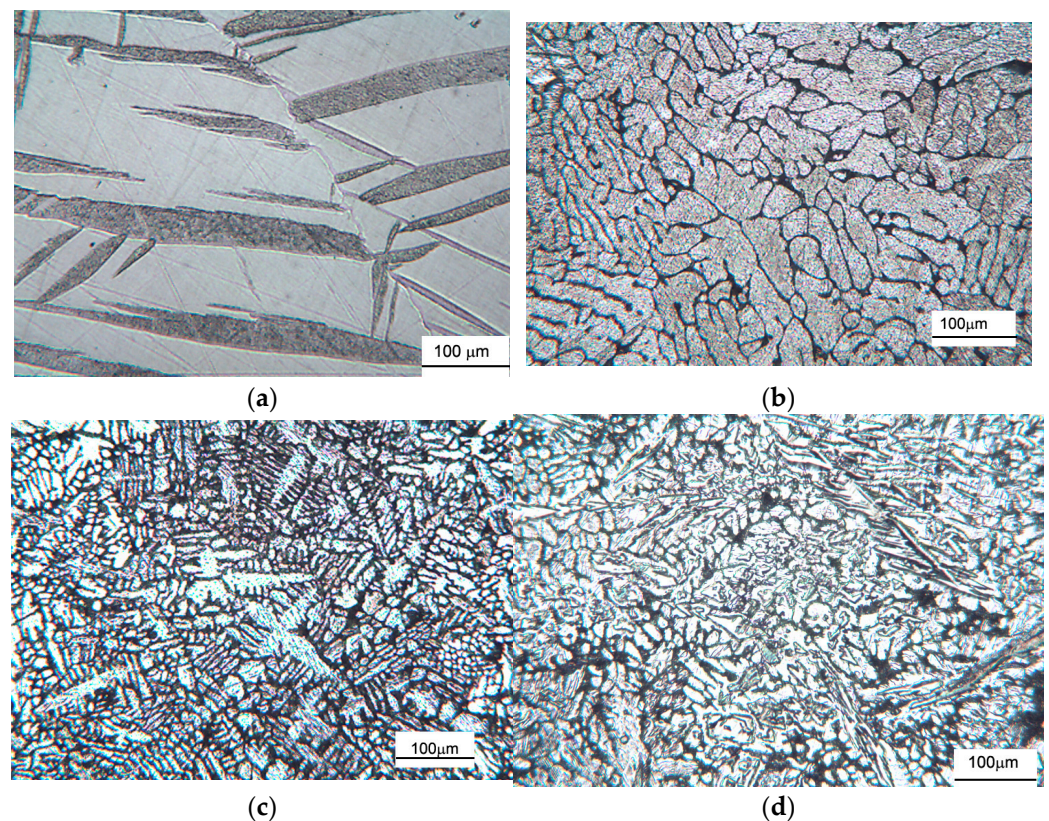


Figure 3. Optical micrographs of the experimental alloy microstructures: (a) Zn–0.00Ti; (b) Zn–0.10Ti; (c) Zn–0.25Ti; (d) Zn–1.00Ti.

In Figure 3b, the microstructure of the as-cast Zn–0.10Ti is characterised by an α -Zn dendritic morphology, with the average grain size decreasing to approximately $200 (\pm 50) \mu\text{m}$. Also, the dendritic arm size in relation with the relatively low solidification rate and low Ti content has values in the 20–70 μm range with a shape ratio between 0.3 and 0.5. As it is observed from the Zn–Ti binary phase diagram (Figure 1), the Zn–0.1 wt.% Ti alloy is a hypoeutectic alloy. It can be considered that the Zn–0.10Ti alloy comprises primary Zn dendrites and a eutectic of Zn and intermetallic phase mixtures (TiZn_{16}) placed in the interdendritic space of primary α -Zn as it is confirmed by the OM from Figure 3b.

Analysing the microstructure from Figure 3c, the OM of the as-cast Zn–0.25Ti shows a decreasing grain size compared to the as-cast pure Zn and Zn–0.10Ti. The average grain size decreases to approximately $100 (\pm 27) \mu\text{m}$ with the Ti content increasing from 0.10 to 0.25 wt.%. Given the low solidification rate and higher Ti content above but close to the (α -Zn + TiZn_{16}) eutectic Ti content (approximately 0.16 wt.% Ti), Zn–0.25Ti can be considered as a hypereutectic alloy. The (α -Zn + TiZn_{16}) eutectic morphology has, as the main feature, the relative coarse lamella of α -Zn phase in eutectic and small and rare primary TiZn_{16} .

Zn–1.00Ti is also a hypereutectic alloy, but the Ti content is much higher than the eutectic. The eutectic morphology is different compared to Zn–0.25Ti, with both eutectic regions having finer or larger lamellae of α -Zn, especially the larger primary TiZn_{16} .

3.2.4. SEM Microscopy

The SEM images of the Zn–xTi alloy microstructures are shown in Figure 4a–d, and the same features were observed in the OM images.

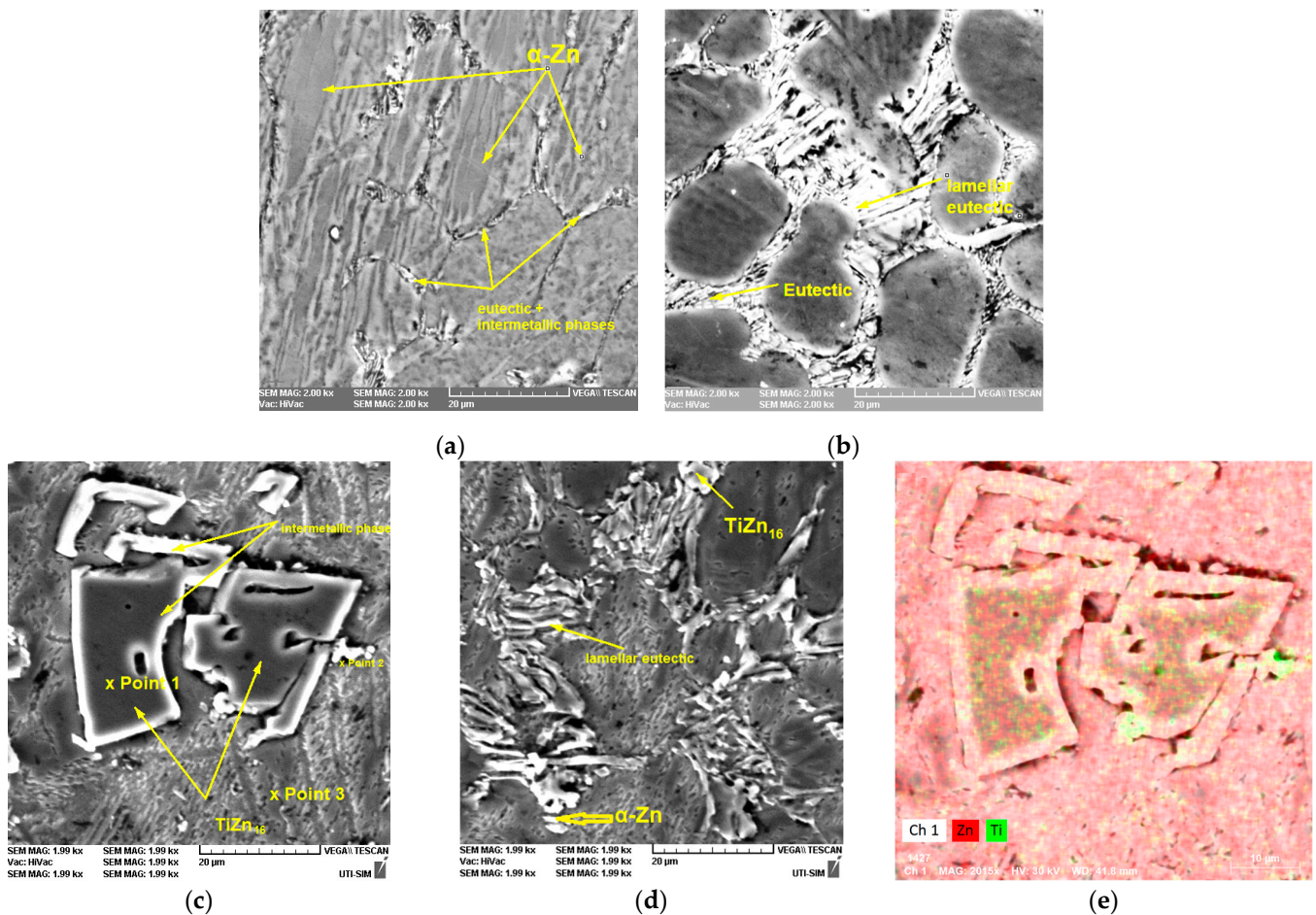


Figure 4. Microstructural and chemical insights of Zn–Ti alloys (a) The Zn–0.10Ti alloy structure; (b) Zn–0.25Ti; (c) Zn–1.00Ti–area1; (d) Zn–1.00Ti–area2 and (e) the elemental distribution of Zn and Ti on the area given in (c).

Supplementary, EDS was performed on three different points (Figure 4c), with 90 nm diameter spots on different structural entities presenting the formation of two different TiZn intermetallic compounds, points 1 and 2 spread in the eutectic matrix and point 3. The energy spectrum obtained from a 4 mm² area confirmed the presence of Zn and Ti elements at different energies.

The Zn and Ti elemental distributions, shown in Figure 4e, confirmed the formation of two TiZn intermetallic compounds. In point 1, a compound with 94.97 (93.26) wt.(at.)% Zn and 5.03 (6.74) wt.(at.)% Ti was observed. The chemical composition corresponds to the TiZn₁₆ phase. In point 2, the chemical composition has an average value of approximately 82.85 (77.95) wt.(at.)% Zn and 17.15 (22.04) wt.(at.)% Ti. According to Vassilev et al., the chemical composition of the compound identified in point 2 is close to the TiZn₃ compound [33], although not identified by XRD analysis, presumably on account of its low volume fraction.

3.3. Mechanical Properties

3.3.1. Compression

The stress–strain compression curves were analysed and interpreted according to ASTM E9-09 [43]. Figure 5 shows representative stress–strain curves recorded for all the alloys investigated and the compression data derived from the stress–strain curves shown in the comparative plots.

The average (st. dev.) values of the yield strength at 0.2% offset (YS_{0.2}) were 111.49 (6.08) MPa, 170.26 (2.48) MPa, 226.13 (10.20) MPa and 248.02 (6.32) MPa for Zn–

0.00Ti, Zn–0.10Ti, Zn–0.25Ti and Zn–1.00Ti. For the same alloys, the average (st. dev.) values of the compressive strength at 50% strain were 361.40 (8.10) MPa, 484.32 (20.14) MPa, 520.55 (19.20) MPa and 524.23 (23.17) MPa. OWR-ANOVA statistical analysis showed that, for both mechanical properties, there were significant differences between the mean values for Zn–0.00Ti, Zn–0.10Ti, Zn–0.25Ti or Zn–1.00Ti. Although the average values for Zn–0.25Ti are lower than those for Zn–1.00Ti alloys, statistically there are no significant differences.

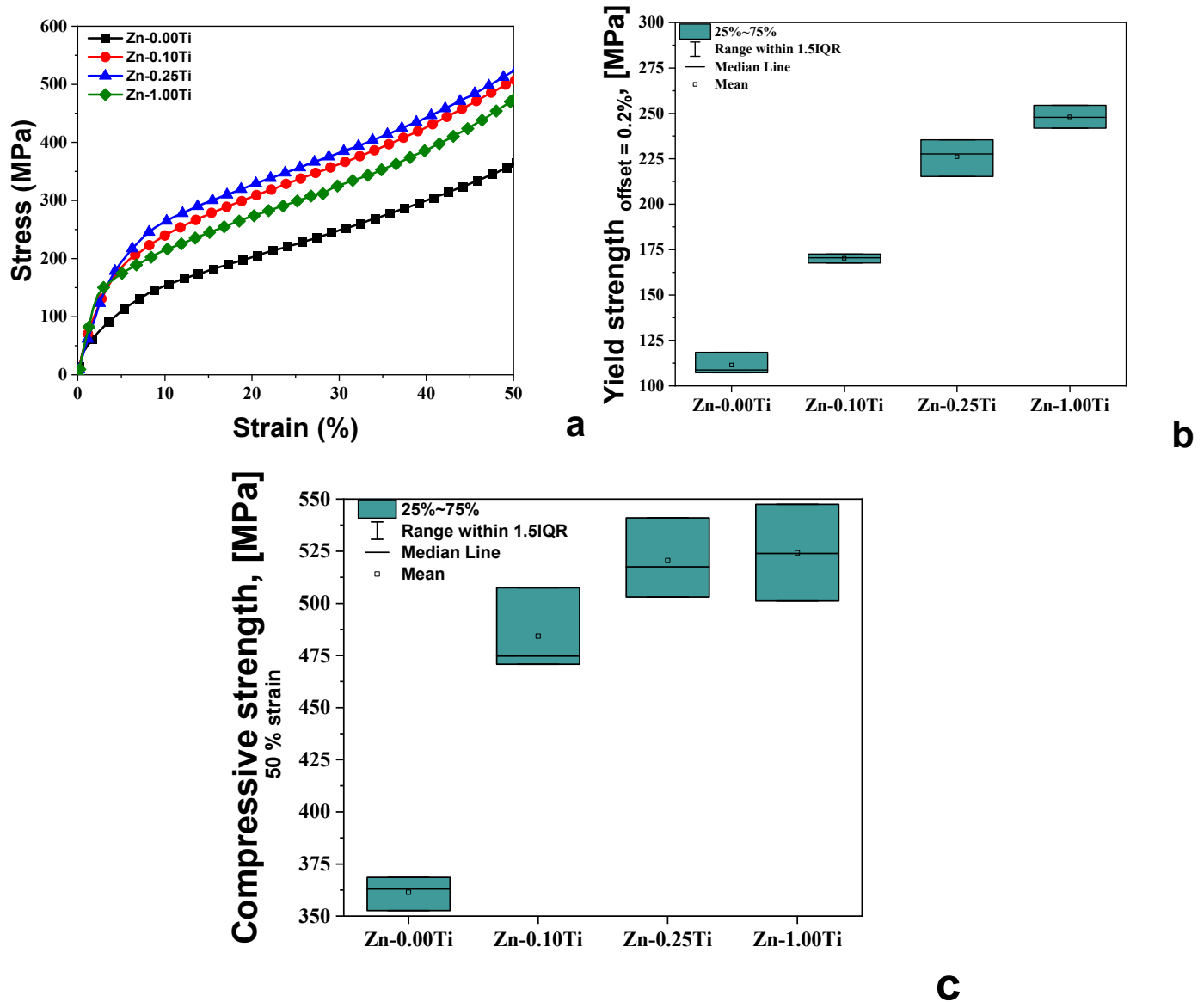


Figure 5. Representative compression curves and data: (a) compression stress–strain representative curves for all Zn–xTi alloys; (b) yield strength (offset = 0.20%); (c) compression strength (50% strain).

3.3.2. Microhardness

The results of the microindentation tests are graphically shown in Figure 6. The average (st. dev.) values of the microhardness were 0.328 (0.037) GPa, 0.531 (0.020) GPa, 0.619 (0.034) GPa and 0.694 (0.023) GPa. Despite the average values increasing with increasing Ti content, the OWR-ANOVA statistical analysis showed that there are significant differences between the average microhardness values of Zn–0.00Ti compared to all other alloys and of Zn–0.10Ti compared to Zn–0.00Ti and Zn–1.00Ti.

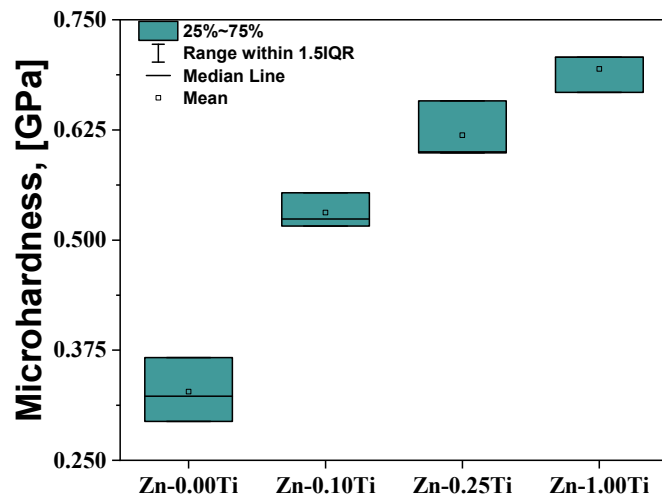


Figure 6. Microhardness results of Zn-xTi alloys.

3.3.3. Friction Properties

Table 2 shows the values of applied force (F) and the mean (st. dev.) values of friction coefficient (COF) and friction force (Ff). The TWR-ANOVA statistical analysis showed that there were significant differences between the average values of COF corresponding to Zn-0.00Ti and Zn-1.00Ti for 10 N applied force, and Zn-0.00Ti, Zn-0.10Ti, Zn-0.25Ti and Zn-1.00Ti, the exception being Zn-0.25Ti and Zn-1.00Ti for 19 N applied force.

Table 2. The average values of the coefficient of friction and force friction.

Alloy	Applied Force, F [N]	COF	Ff, [N]
		Average (St. Dev.)	Average (St. Dev.)
Zn-0.00Ti	10	0.578 (0.327)	3.96 (3.28)
	19	0.804 (0.401)	9.82 (7.67)
Zn-0.10Ti	10	0.422 (0.270)	2.91 (2.92)
	19	0.726 (0.393)	9.16 (7.53)
Zn-0.25Ti	10	0.316 (0.193)	2.12 (2.18)
	19	0.661 (0.423)	8.67 (7.9)
Zn-1.00Ti	10	0.245 (0.154)	1.65 (1.76)
	19	0.622 (0.417)	8.23 (7.69)

Using the COF values from Table 2 and the TWR-ANOVA results, Figure 7 graphically shows the dependence of COF on Ti content and applied force.

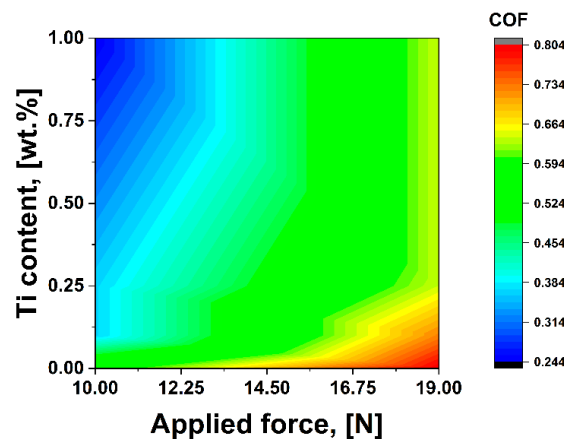


Figure 7. COF vs. applied force and Ti content.

3.4. Degradation Behavior

The corrosion resistance of the alloys was evaluated through immersion and electrochemical tests.

3.4.1. Immersion

When interacting with an electrolyte solution, metallic materials, particularly alloys, undergo an exchange of electrons and ions, causing changes in the chemistry of the metal/electrolyte interface. The chemical processes at the metal/electrolyte interface produce acid/base radicals that lead to passivation of the metal substrate or changes in electrolyte pH, whether the reaction products are soluble or not. For the present study, the pH of the electrochemical solution was recorded during the immersion tests, and its evolution is shown in Figure 8. In addition, the chemical compositions of the corroded surfaces of the Zn-xTi alloys after the immersion tests are shown in Table 3. These measurements were used to investigate the nature of the corrosion products. The degradation rates obtained for the three different immersion intervals are also given in Table 4.

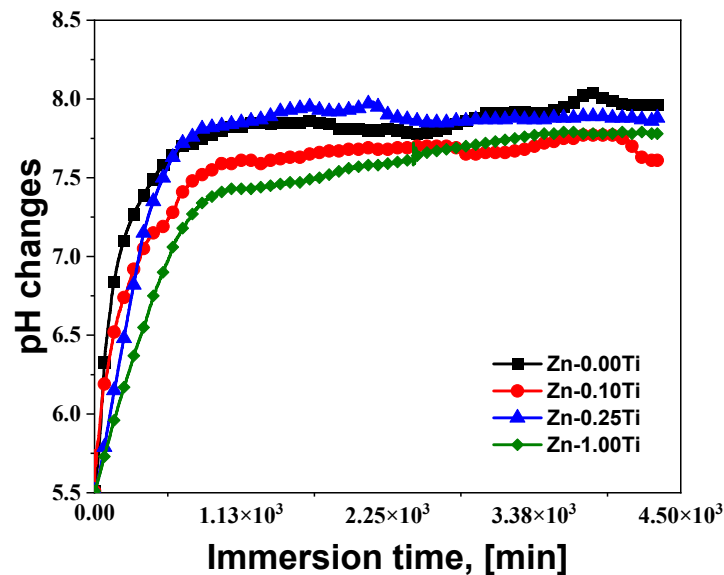


Figure 8. The representative pH variation plots recorded during the immersion tests for 72 h.

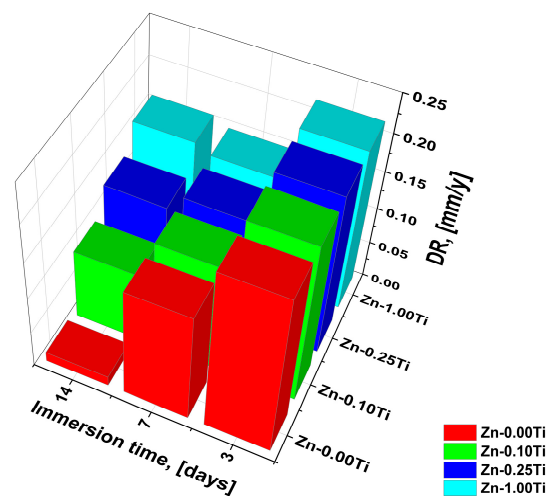
Table 3. The chemical composition of the corroded surfaces for the tested alloys after the immersion intervals.

Time/Samples/Elements		Zn	Ti	O	Na	C	Cl
		at.%	at.%	at.%	at.%	at.%	at.%
3 days	Zn-0.00Ti	24.4	-	43.6	14.7	16.5	0.6
	Zn-0.10Ti	19.5	0.10	46.8	9.9	22.9	0.8
	Zn-0.25Ti	29.6	0.10	37.8	16.5	10.2	5.7
	Zn-1.00Ti	19.4	0.40	46.8	9.2	23.7	0.5
7 days	Zn-0.00Ti	32.8	-	33.8	18.7	13.5	1.2
	Zn-0.10Ti	28.1	0.10	37.9	17.6	15.9	0.5
	Zn-0.25Ti	28.2	0.20	37.4	17.6	16.3	0.4
	Zn-1.00Ti	23.5	0.30	40.6	14.5	20.3	0.8
14 days	Zn-0.00Ti	19.7	-	45.5	11.5	22.4	0.9
	Zn-0.10Ti	28.2	0.02	38.3	21.6	11.3	0.6
	Zn-0.25Ti	25.5	0.03	41.04	15.7	17.2	0.5
	Zn-1.00Ti	25.6	0.2	38.1	18.3	17.7	0.2
St. Dev. %		0.11	0.01	0.61	0.18	0.44	0.06

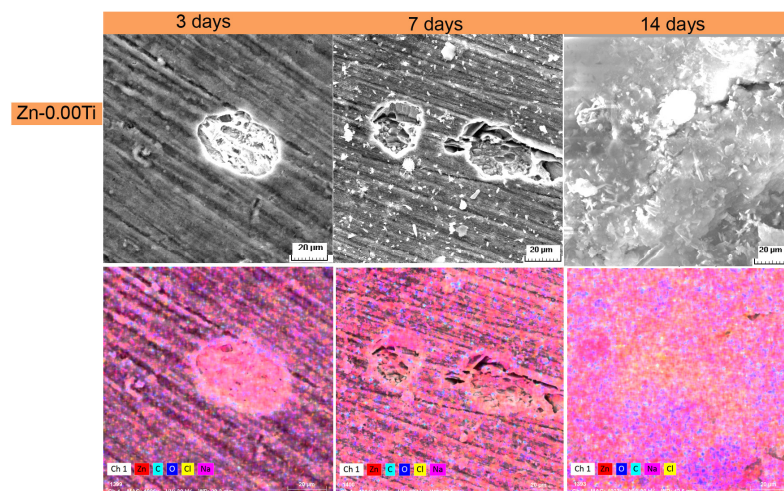
Table 4. Degradation rates determined for all investigated Zn–xTi alloys.

Alloys/Immersion Time	Degradation Rates ($\mu\text{m}/\text{y}$)		
	3 Days	7 Days	14 Days
Zn–0.00Ti	268 (67)	163 (53)	13 (3)
Zn–0.10Ti	226 (11)	179 (2)	128 (5)
Zn–0.25Ti	217 (37)	102 (1)	96 (2)
Zn–1.00Ti	166 (17)	152 (17)	159 (7)

The TWR-ANOVA statistical analysis showed that, for all Zn–xTi alloys, significant differences of DR mean values were found depending on the immersion time. Ti content caused a significant difference after 14 days immersion for Zn–0.10Ti and Zn–1.00Ti. From the DR and TWR-ANOVA mean values, the dependence of DR on Ti content and immersion time is plotted in Figure 9.

**Figure 9.** Degradation rate (DR) variation vs. wt.% Ti and immersion time.

The corroded surfaces of the investigated alloys were analysed by SEM after the three immersion intervals and ultrasonic cleaning to remove the unstable compounds. The results are shown in Figure 10. In the same figure, the distribution of the main elements identified on the surface, Zn, O, Cl, Na and Ti, are also illustrated.

**Figure 10.** *Cont.*

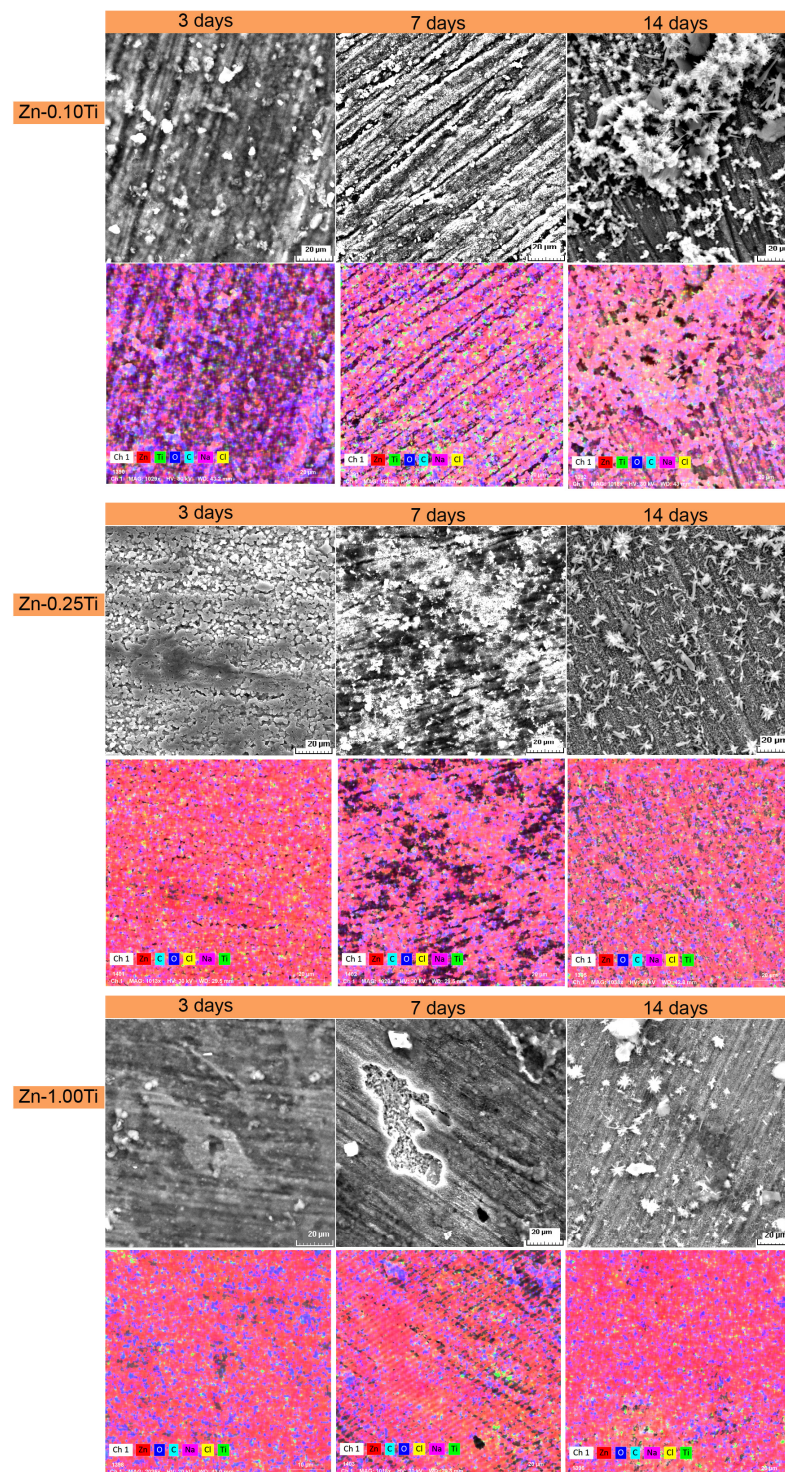


Figure 10. SEM and EDS images of the samples after immersion in NaCl (9 mg) for 3, 7 and 14 days.

3.4.2. Electrochemical Tests

Electrochemical experiments on the open-circuit potential (OCP), linear polarisation and cyclic voltammetry were performed to further investigate the influence of the Ti addition to Zn (Figure 11). Using Tafel extrapolation (Figure 11a), I_{corr} has been evaluated, and degradation (corrosion) rates (DR) have been determined (Table 5).

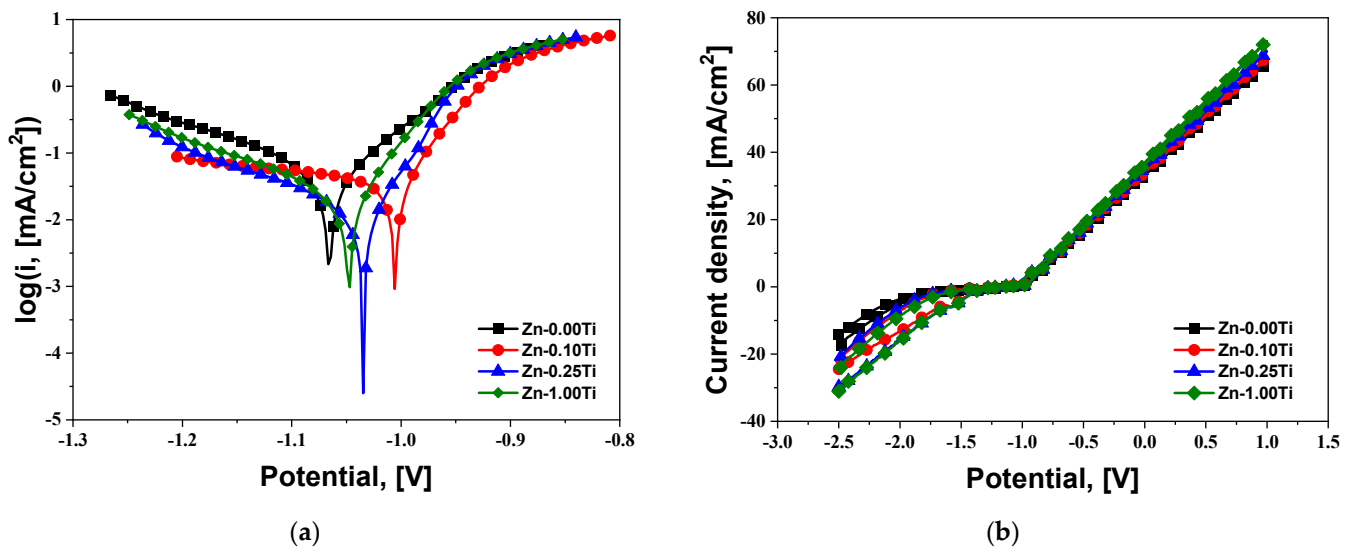


Figure 11. Electro-corrosion results of the experimental alloys in NaCl: (a) Tafel diagrams; (b) voltammograms with cyclic curves.

Table 5. Electrochemical corrosion parameters (in 0.9% NaCl saline solution).

Alloy	Corrosion Process Parameters							
	OCP, [mV]	E (I = 0), [mV]	I_{corr} , [mA/cm ²]	R_p , [Ohm/cm ²]	DR, [$\mu\text{m}/\text{y}$]	β_c , [mV/dec]	β_a , [mV/dec]	OCP, [mV]
Zn-0.00Ti	−1010	−1065.8	0.0625	468.95	934.2	−203.6	93.6	−1060
Zn-0.10Ti	−935	−1005.6	0.0334	645.31	500.0	−496.8	51.8	−1115
Zn-0.25Ti	−1020	−1035.3	0.0162	1430.00	241.9	−197.8	49.7	−1100
Zn-1.00Ti	−990	−1048.4	0.0156	906.85	233.5	−146.5	50.1	−1050

Experimental electrochemical test results show that the Zn-1.00Ti alloy had the lowest corrosion rate, 233.5 $\mu\text{m}/\text{y}$ and current density I_{corr} 0.0156 mA/cm². Linear polarisation curves show no significant changes in the anodic branch caused by the addition of Ti. Cyclic voltammograms show similar characteristics for all Zn-xTi alloys. Furthermore, a passive region between −1.4 and −0.9 V was observed for all alloys.

4. Discussion

The alloying of Zn with Ti resulted in different microstructural features corresponding to the low-Ti region of the binary Zn-Ti phase diagram, affecting the properties of the Zn-xTi alloys, as can be observed from the results on mechanical properties and corrosion behaviour presented above. As the Ti content increased, a different eutectic morphology was observed, and the volume fraction of the TiZn₁₆ intermetallic compound increased continuously (Figure 4a–d). As reported in the literature, the increasing Ti addition caused the modification of the cast cp-Zn to a very coarse grain size (above 1 μm) [44,45], to a hypoeutectic and then two hypereutectic alloys with the formation of primary TiZn₁₆ intermetallic phase [28,39,44] and finer eutectic. As the percentage of Ti increases, the appearance of the lamellar eutectic is observed (Figure 4b) as well as its interruption for higher percentages of Ti (Figure 4d).

The EDS investigation confirmed that primary TiZn₁₆ intermetallic phases were formed in the as-cast Zn-0.25Ti and Zn-1.00Ti alloys (Figure 4d). The chemical composition of the TiZn₁₆ intermetallic compound is approximately 94.97 (93.26) wt.(at.)% Zn and 5.03 (6.74) wt.(at.)% Ti (point 1 from the SEM image in Figure 4c), corresponding to an approximate mole ratio for Zn:Ti of 16:1. As shown in the Zn-Ti phase diagram (Figure 1), it is considered that TiZn₁₆ is the intermetallic compound formed in the Zn-0.25Ti alloy

and Zn–1.00Ti. These results are in agreement with a previous study, which demonstrated the presence of the primary Zn–Ti intermetallic phase in as-cast Zn–Ti alloys (0.16, 0.18, 0.23 and 0.34 wt.% Ti) [27]. By increasing the amount of Ti added to Zn from 0.25 to 1 wt.%, a new intermetallic compound was identified by EDS analysis (point 2 in Figure 4c), TiZn_3 , but without validation on the XRD pattern [33,34].

The higher values of mechanical properties were obtained as the Ti content increased from 0.00 to 1.00 wt.%. However, the increase between 0.25 wt.% and 1.00 wt.% is greater than between 0.00 wt.% and 0.25 wt.%; a smaller increase was observed in the 0.25–1.00 wt.% Ti range. A similar compressive strength value (Figure 5) was measured for a Zn–1 wt.% Ti alloy (approximately 265 MPa) and reported in the literature [46].

The average hardness values of the alloys, based on the results shown in Figure 6, increased upon the addition of a small amount of Ti to cp-Zn. Two main reasons could be identified for the increase in hardness of Zn–xTi compared to the cast cp-Zn. The first is related to the Ti addition resulting in a grain refinement process through the appearance of a eutectic and intermetallic phases at the grain boundaries [47,48]. Secondly, at a higher addition than 0.25 wt.% Ti, the formation of the TiZn_{16} primary intermetallic compound enhanced the hardening of Zn–xTi alloys.

The variation tendency of the friction coefficient is similar to the microhardness but inversely proportional. The friction coefficient of cast cp-Zn decreased by Ti addition. By increasing the Ti content to 1 wt.%, the friction coefficient decreases by 50% at low loads (10 N) and by approximately 25% at higher loads (19 N).

The hydroxide-based compounds formed from the start of the alloy-solution interaction resulted in a constant increase in the pH of the solution. The larger pH variations at the beginning of the immersion, namely the first 5–8 h, can be attributed to a more pronounced electron/ion exchange and the formation of corrosion compounds. In all cases, the pH of the electrolyte solution increases from approximately 5 to 7.5–8.0 as a result of a much more frequent exchange of ions between the immersed metallic material and the solution. After the first hours, a lower intensity in the pH variation is attributed to the stabilisation of the corrosion process, as the alloy is protected by a corrosion compound layer formed during this interval. This is supported by the Pourbaix diagram of Zn. There is also a strong correlation between the electrochemical behaviour associated with Zn corrosion and the pH of the electrolyte. The Pourbaix diagram of Zn in an aqueous environment [49] shows that the Zn can be oxidized to dissolved forms of Zn^{2+} , $\text{Zn}(\text{OH})_2$, HZnO_2^- and ZnO_2^{2-} with increasing pH. The diagram shows the stability of $\text{Zn}(\text{OH})_2$ or ZnO compounds in the range of 6–8 pH.

After the immersion tests, the Zn–xTi alloyed samples showed a higher percentage of oxides formed on the surface after 3 or 7 days of immersion and a lower percentage after 14 days. On the surface of all samples, regardless of the immersion time, Na and Cl were identified as salts formed from the interaction between the alloy and the electrolyte solution or deposited from the NaCl solution (Table 3 and Figure 10). The DRs of the alloys, determined by the mass losses resulting after the three immersion intervals (Equation (1)), show a reduction in the corrosion rate caused by the increase in the oxidized layer on the surface, which correlates with the increase in O wt.% (Figure 9 and Tables 3 and 4). This pattern, observed in all cases, is inferior for the Zn–1.00Ti alloy, where the determined degradation rates are more similar for all immersion intervals (Table 4 and Figure 9), attributed to the influence of titanium on the corrosion rate of pure zinc through the formation of a eutectic between α -Zn and the TiZn_{16} intermetallic compound. The degradation rate results are consistent with those reported by Liu et al. (2019) [50] for pure Zn. In addition to the constituent elements Zn and Ti, the oxygen responsible for the oxide layer formation and the other elements identified resulted from compounds that remained on the surface, mostly in the corrosion traces that emerged and were not removed by ultrasonic cleaning. The corrosion and degradation of the alloys occurred progressively by the repeated removal of layers that reached an advanced degree of oxidation, losing their stability and mechanical integrity and entering the electrolyte solution as reactive compounds [51,52]. Furthermore,

the addition of at least 1% Ti decreased the DR due to the titanium oxide formed on the surface in contrast to the degradation rate of Zn–0.00Ti (as-cast cp-Zn) (Table 4).

Zinc and zinc-based alloys are very active metals in ionic media, especially in the presence of chloride ions.

Tafel slopes provide information on the reaction mechanism (Figure 11a). In this case, the small value of the anodic slope indicates the following reaction:



The above active reaction is controlled only by concentration, while the cathodic reaction is slower and controls the overall corrosion rate. The control of activation is determined by the electron transfer rate from the anode to the cathode (Figure 12).

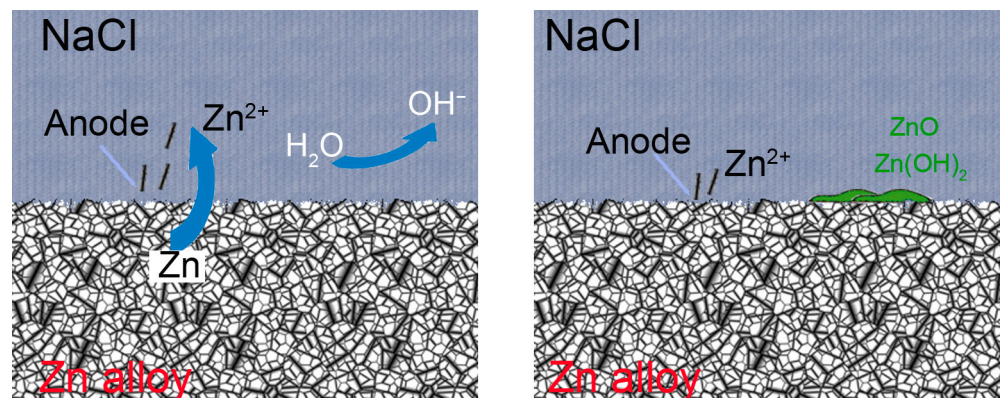


Figure 12. Schematic representation of the corrosion mechanism of zinc alloy surfaces in NaCl solution.

In the presence of dissolved oxygen at the cathode, the following Reaction (4) occurs:



Followed by the Reactions (5) and (6):



Corrosion potential (E), corrosion current density, (I_{corr}), anodic Tafel slope (β_a) and cathodic Tafel slope (β_c) are parameters calculated by the Tafel extrapolation (Table 5). The corrosion rate varies between 233.5 [$\mu\text{m}/\text{y}$] for Zn–1.00Ti and 934.2 [$\mu\text{m}/\text{y}$] for Zn–0.00Ti. It decreases with increasing Ti percentage, which means that the newly formed intermetallic compound ZnTi_{16} increases corrosion resistance. The corrosion current density (I_{corr}) also decreases with increasing percentage of Ti from 0.0625 [mA/cm^2] to 0.0156 [mA/cm^2]. This is believed to be caused by the stability of the corrosion product layers. In the NaCl solution, the corrosion potential of Zn alloy is approximately 1.00 V lower than the corrosion potential reported in potentiodynamic tests of Zn alloys in SBF [53].

The cyclic voltammograms of the four alloys shown in Figure 11b are all similar in patterning. For all curves, the linear current–voltage dependence starts at an overpotential of -1000 mV. It can be observed that the reverse branch (cathodic curve) overlaps almost perfectly with the direct branch (anodic curve). Therefore, the generalised corrosion caused by the overpotential does not significantly alter the active surface nor causes passivation through the deposition of reaction products. It may be explained by the formation of OH^- ions, which leads to an increase in the pH; consequently, the formation of zinc hydroxide chloride on the surface alloys confirms the results shown in Figure 8.

5. Conclusions

In this study, titanium was used as the alloying element to design the Zn–xTi (x = 0.1, 0.25 and 1.0 wt.%) series of alloys. Their microstructure, mechanical properties and corrosion behaviour have been systematically analysed. The main conclusions are as follows:

- For contents higher than 0.25 wt.% Ti, the formation of a primary TiZn₁₆ intermetallic compound in the (α -Zn + TiZn₁₆) eutectic matrix is observed both by X-ray diffraction and by structural and chemical analyses. Alloying with Ti leads to refinement of α -Zn dendrites for hypoeutectic alloys and refinement of eutectic grains for hypereutectic alloys. These changes in microstructural features led to an improvement in the mechanical properties of Zn–xTi alloys.
- After the interaction between the alloys and the saline solution, the pH increased after the first hours (10–15 h) and then remained stable between 7.5 and 8, but different values of the degradation rate were observed, decreasing for Zn–0.00Ti (as-cast cp-Zn) and remaining almost constant for Zn–1.00Ti.
- Electrochemical tests performed following immersion, i.e., at a pH of approximately 5.5–6.0, showed that the degradation rate decreased as the Ti content increased.

Author Contributions: Conceptualization, R.C. (Romeu Chelariu), N.C. and A.-T.Ş.; methodology, R.C. (Ramona Cimpoeşu), B.I. and A.-M.R.; software, M.M.; validation, R.C. (Romeu Chelariu), G.Z. and A.A.; formal analysis, V.G., B.I. and M.B.; investigation, R.C. (Ramona Cimpoeşu), N.C., A.-M.R., M.M. and M.B.; resources, A.-T.Ş.; data curation, V.G.; writing—original draft preparation, R.C. (Romeu Chelariu), N.C. and A.-T.Ş.; writing—review and editing, M.M., B.I. and V.G.; visualization, R.C. (Ramona Cimpoeşu) and B.I.; supervision, G.Z., N.C. and M.M.; project administration, N.C., M.B. and A.A. All authors have read and agreed to the published version of the manuscript.

Funding: This work was supported by a National Research Grants of the TUIASI, project number GNaC2023_285/2024.

Data Availability Statement: The original contributions presented in the study are included in the article, further inquiries can be directed to the corresponding author.

Conflicts of Interest: The authors declare no conflict of interest.

References

1. Hermawan, H. Updates on the research and development of absorbable metals for biomedical applications. *Prog. Biomater.* **2018**, *7*, 93–110. [[CrossRef](#)] [[PubMed](#)]
2. Li, C.; Guo, C.; Fitzpatrick, V.; Ibrahim, A.; Zwierstra, M.J.; Hanna, P.; Lechtig, A.; Nazarian, A.; Lin, S.J.; Kaplan, D.L. Design of biodegradable, implantable devices towards clinical translation. *Nat. Rev. Mater.* **2020**, *5*, 61–81. [[CrossRef](#)]
3. Khan, A.R.; Grewal, N.S.; Zhou, C.; Yuan, K.; Zhang, H.J.; Jun, Z. Recent advances in biodegradable metals for implant applications: Exploring in vivo and in vitro responses. *Results Eng.* **2023**, *20*, 101526. [[CrossRef](#)]
4. Yang, H.; Lin, W.; Zheng, Y. Advances and perspective on the translational medicine of biodegradable metals. *Biomater. Transl.* **2021**, *2*, 177–187. [[PubMed](#)]
5. Wanga, J.; Doua, J.; Wanga, Z.; Hua, C.; Yub, H.; Chen, C. Research progress of biodegradable magnesium-based biomedical materials: A review. *J. Alloys Compd.* **2022**, *923*, 166377. [[CrossRef](#)]
6. Rabeeh, V.P.M.; Hanas, T. Progress in manufacturing and processing of degradable Fe-based implants: A review. *Prog. Biomater.* **2022**, *11*, 163–191. [[CrossRef](#)]
7. Nriagu, J. Zn toxicity in humans. In *Encyclopedia of Environmental Health*; Elsevier: Amsterdam, The Netherlands, 2011; pp. 801–807.
8. Plum, L.M.; Rink, L.; Haase, H. The Essential Toxin: Impact of Zinc on Human Health. *Int. J. Environ. Res. Public Health* **2010**, *7*, 1342–1365. [[CrossRef](#)] [[PubMed](#)]
9. Sangeetha, V.J.; Dutta, S.; Moses, J.A.; Anandharamakrishnan, C. Zinc nutrition and human health: Overview and implications. *eFood* **2022**, *3*, e17. [[CrossRef](#)]
10. Chasapis, C.T.; Loutsidou, A.C.; Spiliopoulou, C.A.; Stefanidou, M.E. Zinc and human health: An update. *Arch. Toxicol.* **2012**, *86*, 521–534. [[CrossRef](#)]
11. Jomova, K.; Makova, M.; Alomar, S.Y.; Alwasel, S.H.; Nepovimova, E.; Kuca, K.; Rhodes, C.J.; Valko, M. Essential metals in health and disease. *Chem. Biol. Interact.* **2022**, *367*, 110173. [[CrossRef](#)]
12. Kim, T.; Wang See, C.; Li, X.; Zhu, D. Orthopedic implants and devices for bone fractures and defects: Past, present and perspective. *Eng. Regen.* **2020**, *1*, 6–18. [[CrossRef](#)]

13. Chen, K.; Gu, X.; Zheng, Y. Feasibility, challenges and future prospects of biodegradable zinc alloys as orthopedic internal fixation implants. *Smart Mater. Manuf.* **2024**, *2*, 100042. [[CrossRef](#)]
14. Wang, X.; Lu, H.; Li, X.; Li, L.; Zheng, Y. Effect of cooling rate and composition on microstructures and properties of Zn-Mg alloys. *Trans. Nonferrous Met. Soc. China* **2007**, *17*, s122–s125.
15. Vojtech, D.; Kubásek, J.; Šerák, J.; Novák, P. Mechanical and corrosion properties of newly developed biodegradable Zn-based alloys for bone fixation. *Acta Biomater.* **2011**, *7*, 3515–3522. [[CrossRef](#)]
16. Zhuo, X.; Wu, Y.; Ju, J.; Liu, H.; Jiang, J.; Hu, Z.; Bai, J.; Xue, F. Recent progress of novel biodegradable zinc alloys: From the perspective of strengthening and toughening. *J. Mater. Res. Technol.* **2022**, *17*, 244–269. [[CrossRef](#)]
17. Liu, Y.; Du, T.; Qiao, A.; Mu, Y.; Yang, H. Zinc-Based Biodegradable Materials for Orthopaedic Internal Fixation. *J. Funct. Biomater.* **2022**, *13*, 164. [[CrossRef](#)]
18. Kong, L.; Heydari, Z.; Lami, G.H.; Saberi, A.; Baltatu, M.S.; Vizureanu, P. A Comprehensive Review of the Current Research Status of Biodegradable Zinc Alloys and Composites for Biomedical Applications. *Materials* **2023**, *16*, 4797. [[CrossRef](#)]
19. Hussain, M.; Ullah, S.; Raza, M.R.; Abbas, N.; Ali, A. Recent Developments in Zn-Based Biodegradable Materials for Biomedical Applications. *J. Funct. Biomater.* **2023**, *14*, 1. [[CrossRef](#)]
20. Shishir, R.; Nasiruddin, U.; Manojkumar, P.; Lokeshkumar, E.; Ponnillavan, V.; Parfenov, E.V.; Valiev, R.Z.; Rameshbabu, N. Zinc as a potential bio-degradable temporary implant material. *Mater. Today Proc.* **2023**, *in press*. [[CrossRef](#)]
21. Yang, H.; Jia, B.; Zhang, Z.; Qu, X.; Li, G.; Lin, W.; Zhu, D.; Dai, K.; Zheng, Y. Alloying design of biodegradable zinc as promising bone implants for load-bearing applications. *Nat. Commun.* **2020**, *11*, 401. [[CrossRef](#)] [[PubMed](#)]
22. Baker, H. Alloy Phase Diagrams. In *ASM Handbook*; ASM International: Materials Park, OH, USA, 1992; Volume 3.
23. Yin, Z.Y. Microstructural Evolution and Mechanical Properties of Zn–Ti Alloys for Biodegradable Stent Applications. Master’s Thesis, Michigan Technological University, Houghton, MI, USA, 2017.
24. Wang, K.; Tong, X.; Lin, J.; Wei, A.; Li, Y.; Dargusch, M.; Wen, C. Binary Zn–Ti alloys for orthopedic applications: Corrosion and degradation behaviors, friction and wear performance, and cytotoxicity. *J. Mater. Sci. Technol.* **2021**, *74*, 216–229. [[CrossRef](#)]
25. ASTM G31-21; Standard Guide for Laboratory Immersion Corrosion Testing of Metals. ASTM International: West Conshohocken, PA, USA, 2021.
26. Bernevig-Sava, M.A.; Darabont, D.C.; Lohan, M.; Mihalache, E.; Bejinariu, C. Selection and verification of personal protective equipment in the context of current legal requirements. *Qual.-Access Success* **2019**, *20*, 109.
27. Spittle, J.A. The Effects of Composition and Cooling Rate on the as-Cast Microstructures of Zn-Ti Alloys. *Metallography* **1972**, *5*, 423–447. [[CrossRef](#)]
28. Goto, S.; Esashi, K.; Koda, S.; Morozumi, S. Structure-Controlling of Zn-Ti Hyper-Eutectic Alloys by Unidirectionally Solidification. *J. Jpn. I Met. Mat.* **1973**, *37*, 466–473.
29. Spittle, J.A. Lamellar and Rod Morphologies in the Zn-TiZn₁₅ Eutectic. *Metallography* **1973**, *6*, 115–121. [[CrossRef](#)]
30. Leone, G.L.; Kerr, H.W. Grain structures and coupled growth in Zn-Ti alloys. *J. Cryst. Growth* **1976**, *32*, 111–116. [[CrossRef](#)]
31. Murray, J.L. The Ti-Zn (Titanium-Zinc) System. *Bull. Alloy Phase Diagr.* **1984**, *5*, 52–56. [[CrossRef](#)]
32. Vassilev, G.P.; Liu, X.J.; Ishida, K. Reaction kinetics and phase diagram studies in the Ti–Zn system. *J. Alloys Compd.* **2004**, *375*, 162–170. [[CrossRef](#)]
33. Vassilev, G.P. Contribution to the zinc-rich side of the Ti–Zn system. *Z. Metallkd.* **2004**, *95*, 813–817. [[CrossRef](#)]
34. Okamoto, H. Ti-Zn (Titanium-Zinc). *J. Phase Equilib. Diff.* **2008**, *29*, 211–212. [[CrossRef](#)]
35. Yang, S.; Su, X.; Wang, J.; Yin, F.; Li, Z.; Tu, H.; Peng, H. The Zn-rich corner of the Zn–Al–Ti system at 723 K. *J. Alloys Compd.* **2010**, *499*, 194–199. [[CrossRef](#)]
36. Chen, X.; Jeitschko, W.; Danebrock, M.E.; Evers, B.H.; Wagner, K. Preparation, Properties, and Crystal Structures of Ti₃Zn₂₂ and TiZn₁₆. *J. Solid State Chem.* **1995**, *118*, 219–226. [[CrossRef](#)]
37. Boczkal, G.; Mikułowski, B.; Wolczynski, W. Oscillatory structure of the Zn-Cu-Ti single crystals. *Mater. Sci. Forum.* **2010**, *649*, 113–118. [[CrossRef](#)]
38. Boczkal, G. Second phase morphology in the Zn-Ti_{0.1}-Cu_{0.1} single crystals obtained at different growth rates. *Arch. Metall. Mater.* **2012**, *57*, 479–484. [[CrossRef](#)]
39. Boczkal, G. Structure and properties of Zn-Ti_{0.2}-Cu_{0.15} single crystal containing eutectic precipitates. *Arch. Metall. Mater.* **2013**, *58*, 1019–1022. [[CrossRef](#)]
40. Jette, E.R.; Foote, F. Precision determination of lattice constants. *J. Chem. Phys.* **1935**, *3*, 605–616. [[CrossRef](#)]
41. Farrar, R.A.; King, H.W. Axial ratios and solubility limits of H.C.P. eta and epsilon phases in the systems Cd–Mn and Zn–Mn. *Metallography* **1970**, *3*, 61–70. [[CrossRef](#)]
42. Saillard, M.; Develey, G.; Beclé, C. The Structure of TiZn₁₆. *Acta Cryst. B* **1981**, *37*, 224–226. [[CrossRef](#)]
43. ASTM E9-09; Standard Test Methods of Compression Testing of Metallic Materials at Room Temperature. ASTM International: West Conshohocken, PA, USA, 2018.
44. Mostaed, E.; Sikora-Jasinska, M.; Mostaed, A.; Loffredo, S.; Demir, A.G.; Previtali, B.; Mantovani, D.; Beanland, R.; Vedani, M. Novel Zn-based alloys for biodegradable stent applications: Design, development and in vitro degradation. *J. Mech. Behav. Biomed. Mater.* **2016**, *60*, 581–602. [[CrossRef](#)] [[PubMed](#)]

45. Sikora-Jasinska, M.; Mostaed, E.; Mostaed, A.; Beanland, R.; Mantovani, D.; Vedani, M. Fabrication, mechanical properties and in vitro degradation behavior of newly developed Zn Ag alloys for degradable implant applications. *Mater. Sci. Eng. C* **2017**, *77*, 1170–1181. [[CrossRef](#)]
46. Zhang, S.; Yuan, P.; Wang, X.; Wang, T.; Zhao, L.; Cui, C. Fabrication and Properties of Zn-3Mg-1Ti Alloy as a Potential Biodegradable Implant Material. *Materials* **2022**, *15*, 940. [[CrossRef](#)]
47. Manasijević, D.; Balanović, L.; Marković, I.; Minić, D.; Premović, M.; Đorđević, A.; Gorgievski, M.; Stamenković, U. Microstructure and thermal properties of the Bi–Ag alloys. *J. Therm. Anal. Calorim.* **2022**, *147*, 1965–1972. [[CrossRef](#)]
48. Anderson, E.A.; Boyle, E.J.; Ramsey, P.W. Rolled Zinc-titanium Alloys. *Trans. Am. Inst. Min. Metall. Eng.* **1944**, *156*, 278–287.
49. Guo, X.; He, G. Opportunities and challenges of zinc anodes in rechargeable aqueous batteries. *J. Mater. Chem. A* **2023**, *11*, 11987–12001. [[CrossRef](#)]
50. Liu, X.; Yang, H.; Xiong, P.; Li, W.; Huang, H.H.; Zheng, Y. Comparative studies of Tris-HCl, HEPES and NaHCO₃/CO₂ buffer systems on the biodegradation behaviour of pure Zn in NaCl and SBF solutions. *Corros. Sci.* **2019**, *157*, 205–219. [[CrossRef](#)]
51. Panaghie, C.; Zegan, G.; Sodor, A.; Cimpoesu, N.; Lohan, N.M.; Istrate, B.; Roman, A.M.; Ioanid, N. Analysis of Degradation Products of Biodegradable ZnMgY Alloy. *Materials* **2023**, *16*, 3092. [[CrossRef](#)]
52. Panaghie, C.; Cimpoesu, R.; Istrate, B.; Cimpoesu, N.; Bernevig, M.A.; Zegan, G.; Roman, A.M.; Chelariu, R.; Sodor, A. New Zn3Mg-xy alloys: Characteristics, microstructural evolution and corrosion behavior. *Materials* **2021**, *14*, 2505. [[CrossRef](#)] [[PubMed](#)]
53. Gerhátová, Ž.; Babincová, P.; Drienovský, M.; Pašák, M.; Cernicková, I.; Duriška, L.; Havlík, R.; Palcut, M. Microstructure and Corrosion Behavior of Sn–Zn Alloys. *Materials* **2022**, *15*, 7210. [[CrossRef](#)] [[PubMed](#)]

Disclaimer/Publisher’s Note: The statements, opinions and data contained in all publications are solely those of the individual author(s) and contributor(s) and not of MDPI and/or the editor(s). MDPI and/or the editor(s) disclaim responsibility for any injury to people or property resulting from any ideas, methods, instructions or products referred to in the content.